8-1-2011

A HIGH STRAIN-RATE CONSTITUTIVE MODEL FOR SAND WITH APPLICATION IN FINITE ELEMENT ANALYSIS Internal Geotechnical Report 2011-4

William Higgins
University of Connecticut - Storrs, william.higgins@uconn.edu

Dipanjan Basu
University of Connecticut - Storrs, basu.dipan@gmail.com

A HIGH STRAIN-RATE CONSTITUTIVE MODEL FOR SAND WITH APPLICATION IN FINITE ELEMENT ANALYSIS

Internal Geotechnical Report 2011-4

William Higgins and Dipanjan Basu

Department of Civil and Environmental Engineering
University of Connecticut

Storrs, Connecticut

August 2011

SYNOPSIS

The report presents a constitutive model for simulating the high strain-rate behavior of sands. Based on the concepts of critical-state soil mechanics, the bounding surface plasticity theory and the overstress theory of viscoplasticity, the constitutive model simulates the high strain-rate behavior of sands under uniaxial, triaxial and multi-axial loading conditions. The model parameters are determined for Ottawa and Fontainebleau sands, and the performance of the model under extreme transient loading conditions is demonstrated through simulations of split Hopkinson pressure bar tests up to a strain rate of 2000/sec. The constitutive model is implemented in a finite element analysis software to analyze underground tunnels in sand subjected to internal blast loads. Parametric studies are conducted to examine the effect of relative density and type of sand and of the depth of tunnel on the variation of stresses and deformations in the soil adjacent to the tunnels.

KEYWORDS: constitutive model, sand, high strain rate, tunnel, finite element analysis, blast

INTRODUCTION

The development of sustainable and resilient civil infrastructure requires that structures can not only withstand anticipated design loads but also encounter extreme and unanticipated loads with minimal endangerment of individuals and properties. Extreme loading can be caused by nature in the form of tornados, tsunamis or earthquakes or by human activities such as bomb blasts, collisions or industrial accidents. A common feature of these extreme loading scenarios is that they can create very large strains in the surrounding material in a very short period of time. Because so many structures interact with soil, it is necessary to be able to model the effect of these extreme, high-rate loads on soil.

High strain-rate behavior of soil has been studied in the laboratory under triaxial and uniaxial conditions using various testing apparatus (Cassagrande and Shannon 1948, Jackson et al. 1980). The principal observation of the effect of strain rate on sand is that the faster the strain rate is the greater the stiffness and strength are. The increase in strength is manifested through an increase in the peak stress and initial stiffness (Lee et al. 1969). The peak stress also occurs at lesser values of strain as the applied strain rate increases. The effect of increased strength and stiffness is more pronounced in samples with greater relative density and confining stress (Lee et al. 1969, Seed and Lundgren 1954, Whitman and Healy 1962, Yamamuro and Abrantes 2003). In addition to triaxial compression and uniaxial strain tests, projectile methods such as the split Hopkinson pressure bar (SHPB) test (Felice 1985, Veyera and Ross 1995, Song et al. 2009, Martin et al. 2009) have also been used to understand sand behavior under very high strain rate of the order 1000 per second.

A limited number of soil constitutive models have been developed to numerically simulate the high strain-rate behavior of soil. These include the three-phase equation-of-state (EOS) models of Wang et al. (2004), Laine and Sandvik (2001) and Tong and Tuan (2007). The EOS soil models take into account the different speeds of shock wave in the solid, water and air phases of soil. In order to model the solid phase, Tong and Tuan (2007) incorporated Perzyna's viscoplastic flow rule in the Drucker-Prager failure criterion. The model by Wang et al. (2004) also features the Drucker-Prager yield criterion for the solid phase along with the capability of incorporating filament based damage.

Studies on the analysis of boundary value problems related to the high strain-rate behavior of soil are rather limited in number. An et al. (2011) used the constitutive of Tong and Tuan (2007) for finite element (FE) analysis of blast due to explosives embedded in soil. Nagy et al. (2010) incorporated the Drucker-Prager model in a FE framework and simulated wave propagation through soil due to explosions on the ground surface. Yang et al. (2010) incorporated the soil plasticity model of Krieg (1972) in a FE framework and simulated the propagation of blast wave in soil. Lu et al. (2005) performed a coupled three phase analysis using the FE method to simulate blasts propagating through soil — they used a modified Drucker-Prager model with a yield surface that expands with strain rate and coupled it with a rheological damage model. Bessette (2008) used a three phase soil constitutive model with the FE method to simulate the propagation of blast waves due to the explosion of buried C4. Feldgun et al. (2008a, b) and Karinski et al. (2008) used the variational difference method to analyze underground tunnels and cavities subjected to blast loads.

In this report, a constitutive model is presented that simulates the mechanical behavior of sand subjected to strains applied with a rate of up to 2000/sec. Based on the concepts of critical-state soil mechanics, the bounding surface plasticity theory and the overstress theory of viscoplasticity, the model simulates the high strain-rate behavior of sand under multi-axial loading conditions. The model is based on the rate-independent plasticity model developed by Manzari and Dafalias (1997) and modified by Li and Dafalias (2000), Dafalias et al. (2004) and Loukidis and Salgado (2009). The model parameters are determined for Ottawa and Fontainebleau sands by comparing the simulation results with the experimental data available in the literature. The constitutive model is subsequently used to study the response of tunnels embedded in sandy soil and subjected to internal blast loads. The FE software Abaqus (version 6.9) is used for the analyses. The explosive C4 is simulated with the JWL equation-of-state. Parametric studies are performed to examine the effect of relative density and type of sand and of the depth of tunnel on the variation of stresses and deformations in the soil adjacent to the tunnels.

DEVELOPMENT OF THE CONSTITUTIVE MODEL

Critical State Line

In this constitutive model, the critical-state line in the e-p' (e is the void ratio and p' is the effective mean stress given by $p' = (\sigma'_{11} + \sigma'_{22} + \sigma'_{33})/3$ where σ'_{ij} is the effective Cauchy stress tensor) space is given by (Loukidis 2006)

$$e_c = \Gamma - \lambda \left(\frac{p'}{p_a} \right)^{\zeta} \tag{1}$$

where e_c is the void ratio at the critical state (Figure 1) and p_a is the atmospheric pressure. The parameter Γ is the intercept of the critical-state line on the e axis at zero pressure, and λ and ζ are fitting parameters. When a sand sample with a void ratio e less than its value e_c at the critical state (for the same mean stress p') is sheared, the sample dilates causing an increase in e or p' until the critical-state line is reached. Conversely samples with $e > e_c$ contract with decreasing values of e or p until the critical-state line is reached. This behavior is captured through the use of a state parameter $\psi (= e - e_c)$ — the (positive or negative) sign associated with ψ governs whether the shear induced volumetric strain is contractive or dilative (Been and Jefferies 1985).

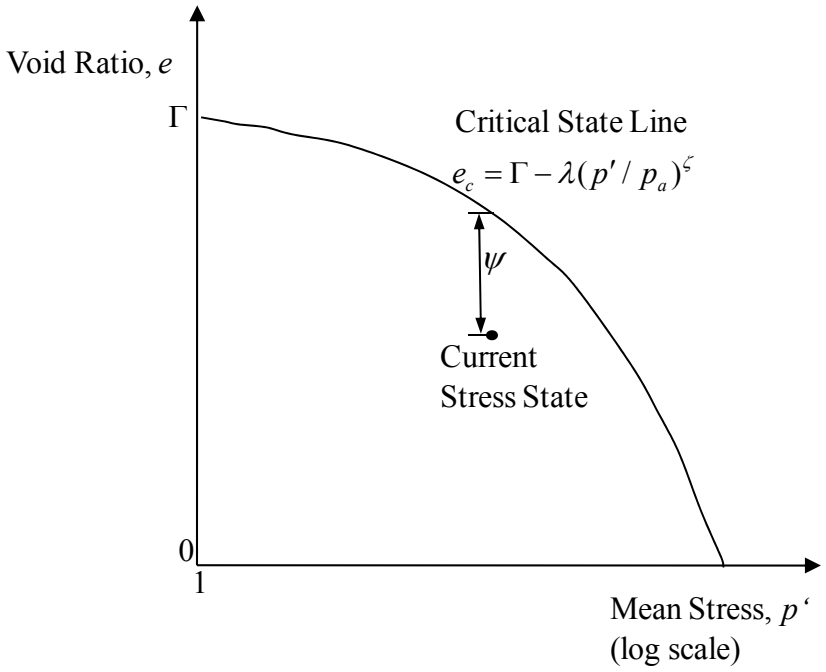

Figure 1. Critical-state line and state parameter

Model Surfaces in Stress-Space

Figure 2 shows the constitutive model surfaces in the principal stress space σ'_1-σ'_2-σ'_3. The model contains four conical shear surfaces — the yield, bounding, dilatancy and critical-state (CS) surfaces — with straight edges in the meridional plane and apex at the origin. The model formulation is done in terms of stress ratios, i.e., stresses normalized with respect p'. The distance of the stress state from the yield surface is described by the yield function f, with the yield surface given by $f = 0$. The yield function in this model is expressed in terms of the deviatoric stress ratio tensor r_{ij} as

$$f = \sqrt{\left(r_{ij} - \alpha_{ij}\right)\left(r_{ij} - \alpha_{ij}\right)}\, p' - \sqrt{2/3}\, mp' \tag{2}$$

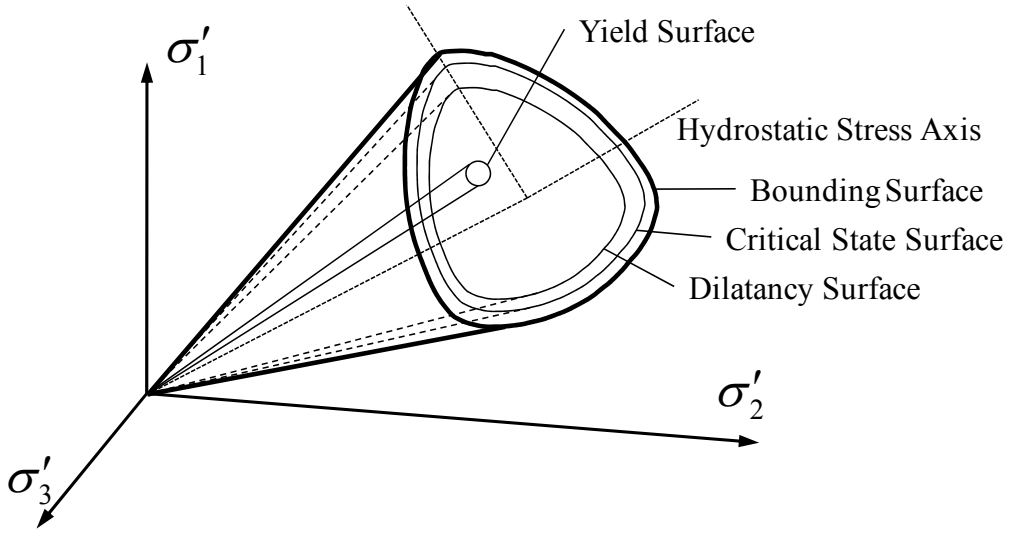

Figure 2. Model surfaces in three dimensional stress space

where m is a model parameter, α_{ij} is the kinematic hardening tensor and $r_{ij} = s_{ij}/p'$ in which s_{ij} (= $\sigma'_{ij} - \delta_{ij}\sigma'_{kk}/3$) is the deviatoric stress tensor (δ_{ij} denotes the Kronecker's delta). The parameters m and α_{ij} have physical meaning in the principal deviatoric stress space s_1-s_2-s_3. The yield surface is a circle in the π-plane of the s_1-s_2-s_3 space with the radius equal to $2m/3$ and the center located at the apex of the "vector" α_{ij} (Higgins 2011). The yield surface cannot harden isotropically (i.e., m is a constant) but can harden kinematically through the evolution of α_{ij} given by

$$\dot{\alpha}_{ij} = \dot{\lambda}\frac{K_P}{p'}\left(\sqrt{\frac{2}{3}}\left(M_b - m\right)n_{ij} - \alpha_{ij}\right)\Bigg/\left(\sqrt{\frac{2}{3}}\left(M_b - m\right) - \alpha_{ij}n_{ij}\right) \tag{3}$$

where $\dot{\lambda}$ is the viscoplastic multiplier, K_P is the viscoplastic modulus, n_{ij} $\left[=\left(s_{ij} - p'\alpha_{ij}\right)/\sqrt{\left(s_{kl} - p'\alpha_{kl}\right)\left(s_{kl} - p'\alpha_{kl}\right)}\right]$ determines the direction of the projection of the current stress state on the critical-state, dilatancy and bounding surfaces (i.e., n_{ij} gives the mapping rule) and M_b is the bounding surface stress ratio in the principal deviatoric stress space given by

$$M_b = g(\theta)M_{cc}e^{(-\psi k_b)} = \left[\frac{\left(1 - \dfrac{1 - c_1^{1/n_s}}{1 + c_1^{1/n_s}}\right)^{n_s}}{\left(1 - \dfrac{1 - c_1^{1/n_s}}{1 + c_1^{1/n_s}}\cos 3\theta\right)^{n_s}}\right]M_{cc}e^{(-\psi k_b)} \tag{4}$$

where k_b is a fitting parameter, M_{cc} is the deviatoric stress ratio q/p' at the critical state under triaxial compression (the deviatoric stress $q = \sqrt{(\sigma_1 - \sigma_2)^2 + (\sigma_1 - \sigma_3)^2 + (\sigma_2 - \sigma_3)^2}\Big/\sqrt{2}$ which simplifies to $q = \sigma_1 - \sigma_3$ for triaxial compression test), $g(\theta)$ is a function of the Lode's angle θ and determines the shape of the critical-state surface in the deviatoric stress space, n_s is an input parameter and

controls the convex shape of the critical-state surface (Loukidis 2006) and C_1 is the ratio of the critical-state stress ratios in triaxial extension and triaxial compression, given by

$$C_1 = \frac{M_{ce}}{M_{cc}} \tag{5}$$

where M_{ce} is the deviatoric stress ratio at the critical state under triaxial extension.

Similar to the bounding surface, the dilatancy surface is also a function of M_{cc} and ψ, and is described by

$$M_d = g(\theta) M_{cc} e^{k_d \psi} \tag{6}$$

where k_d is a fitting parameter. The critical-state surface is described in terms of the generic critical-state ratio M_c given by

$$M_c = M_{cc} g(\theta) \tag{7}$$

Elastic Moduli

The stress-strain relation is given by

$$\dot{\sigma}'_{ij} = 2G\left(\dot{\varepsilon}_{ij} - \dot{\varepsilon}^{vp}_{ij}\right) + \left(K - \frac{2}{3}G\right)\left(\dot{\varepsilon}_{kk} - \dot{\varepsilon}^{vp}_{kk}\right)\delta_{ij} \tag{8}$$

where $\dot{\sigma}'_{ij}$ is the stress increment, $\dot{\varepsilon}_{ij}$ is the total strain increment, $\dot{\varepsilon}^{vp}_{ij}$ is the viscoplastic strain increment, $\dot{\varepsilon}_{kk}$ and $\dot{\varepsilon}^{vp}_{kk}$ are the total and viscoplastic volumetric strain increments, respectively, and K and G are the bulk and shear moduli, respectively. The shear modulus is given by (Hardin and Richart 1963)

$$G = C_g \frac{\left(e_g - e\right)^2}{1+e} \left(p'\right)^{n_g} p_a^{1-n_g} \tag{9}$$

where C_g, n_g and e_g are input parameters. The bulk modulus is related to the shear modulus through a constant Poisson's ratio ν as

$$K = G\frac{2+2\nu}{3-6\nu} \tag{10}$$

When the stress state is entirely within the yield surface, there is no viscoplastic strain in the soil. However, because the yield surface is very small in this model, the viscoplastic process is prevalent for almost the entire loading duration.

Viscoplastic Strain

The total strain is divided into an elastic and a viscoplastic part, and is given by

$$\dot{\varepsilon}_{ij} = \dot{\varepsilon}_{ij}^{e} + \dot{\varepsilon}_{ij}^{vp} \tag{11}$$

where $\dot{\varepsilon}_{ij}^{e}$ is the elastic strain increment. When the stress state reaches or crosses the yield surface, the material undergoes viscoplastic strain. In this model, the overstress theory of Perzyna (1963 and 1966) is used to model the viscoplastic behavior of sand. The overstress theory is based on the viscoplastic overstress function Φ defined as

$$\left\langle \Phi\left(\mathrm{F}\right)\right\rangle = \begin{cases} \mathrm{F} \text{ if } \mathrm{F} > 0 \\ 0 \text{ if } \mathrm{F} \le 0 \end{cases} \tag{12}$$

where the parameter F quantifies the overstress, i.e., the "distance" between the viscoplastic stress state and the yield surface. In this constitutive model, F = f is assumed because, in the cutting plane algorithm used in the implementation of the model, f gives a measure of the distance of the current stress state from the yield surface (Higgins 2011). The magnitude and direction of the viscoplastic strain is determined by the flow rule

$$\dot{\varepsilon}_{ij}^{vp} = \dot{\lambda} R_{ij} \tag{13}$$

where the viscoplastic multiplier $\dot{\lambda}$ is defined as

$$\dot{\lambda} = \frac{\left\langle \Phi\left(\mathrm{F}\right)\right\rangle}{\eta_v} = \frac{f}{\eta_v} \tag{14}$$

with η_v being the viscoplastic coefficient and R_{ij} is the gradient of the viscoplastic potential surface (Loukidis and Salgado 2009) given by

$$R_{ij} = R'_{ij} + \frac{1}{3} D\delta_{ij} \tag{15}$$

where R'_{ij} is the deviatoric component of the gradient (Dafalias and Manzari 2004) that gives the direction of the deviatoric viscoplastic strain rate and D is the dilatancy that controls the shear-induced volumetric viscoplastic strain rate. In this model, the viscoplastic potential is assumed to be identical with the plastic potential used by Dafalias and Manzari (2004) and Loukidis and Salgado (2009). The dilatancy D is given by (Li and Dafalias 2000)

$$D = \frac{D_0}{M_{cc}} \left(\sqrt{\frac{2}{3}} \left(M_d - m \right) - \alpha_{ij} n_{ij} \right) \tag{16}$$

where D_0 is an input parameter.

Viscoplastic Modulus

The viscoplastic modulus K_P used in equation (3) controls the development of the viscoplastic strain and is expressed as a function of the distance between the current stress state and the bounding surface (Li and Dafalias 2002, Loukidis 2006):

$$K_P = h_0 \frac{G \exp(k_b \psi)}{\left[\frac{3}{2} \sqrt{(r_{ij} - \alpha_{ij,\text{ini}})(r_{ij} - \alpha_{ij,\text{ini}})} \right]^{\mu}} \sqrt{\frac{2}{3}} \left(\sqrt{\frac{2}{3}} (M_b - m) - \alpha_{ij} n_{ij} \right) \tag{17}$$

where μ is an input parameter and $\alpha_{ij,\text{ini}}$ is the initial value of the kinematic hardening tensor. The term $\sqrt{2/3}\left(M_b - m \right) - \alpha_{ij} n_{ij})$ is the distance between the current stress state and the projected stress state on the bounding surface. The parameter h_0 takes into

account the effect of void ratio (loose sand develops viscoplastic strains with more ease than dense sand) and is given by

$$h_0 = \left(\frac{e_{\lim} - e}{h_2} \right)^{h_1} \tag{18}$$

where h_1, h_2 and $e_{\lim}$ are input parameters (Loukidis 2006).

MODEL IMPLEMENTATION USING CUTTING PLANE ALGORITHM

The constitutive model is integrated into the finite element software Abaqus using an extension of the cutting plane algorithm for viscoplasticity proposed by Ortiz and Simo (1986). The cutting plane algorithm is a semi-implicit algorithm that uses explicit elastic predictions with an iterative viscoplastic correction loop.

Figure 3 shows a flowchart of the viscoplastic cutting plane algorithm used in this study. The inputs to the algorithm at any time t are the current values of stress (σ_{ij}), strain (ε_{ij}) and hardening variables ξ_i, all denoted with a superscript t, the applied strain increment $\dot{\varepsilon}_{ij}$ and the time increment dt (dt is controlled from outside of the algorithm either by the user or by the finite element analysis). The prime ($'$) associated with the stress tensor is dropped with the understanding that all the stresses calculated are effective stresses. The calculations begin with an elastic prediction step using the current values of the stress state σ_{ij} and the kinematic hardening variable α_{ij}. Note that α_{ij} is generically denoted by ξ_i in Figure 3 and its evolution (equation (3)) is expressed as a function of a generic tensor h_i. During the elastic prediction step, the stress σ_{ij} is increased based on the assumption that the strain increment $\dot{\varepsilon}_{ij}$ is completely elastic. The stiffness D_{ijkl} used in the elastic prediction is the shear modulus when the deviatoric

stress is calculated from the deviatoric strain and is the bulk modulus when the mean stress is calculated from the volumetric strain. Once the stress and strain increments have been calculated, the tensors are updated. In addition to updating the stresses and strains, parameters such as the void ratio, stress invariants, and the state parameter ψ are also updated (note that D_{ijkl} is not updated and stays at the same value as used during the elastic prediction). Using the new values of σ_{ij} and ξ_i, the position of the stress state relative to the yield surface is checked by calculating the overstress f (= $f^{(i)}$ where the superscript i within parentheses counts the iterations of the viscoplastic correction loop) and comparing it against the yield surface error tolerance *FTOL*, which is a small positive number. If the stress state is within the yield surface or sufficiently close to it such that the yield function is less than or equal to *FTOL* (i.e., $f \le FTOL$), then the increment is accepted and the algorithm is complete. However, if during the elastic prediction step the stress state exceeds the boundary of the yield surface (i.e., $f > FTOL$), then the algorithm enters into an iterative viscoplastic correction loop. The value of *FTOL* can be determined by the user and should be calibrated based on the anticipated levels of stress, the required degree of accuracy and the available computational resources — in this study, a value of 0.1 Pa was used.

In the viscoplastic correction loop, the incremental viscoplastic multiplier is calculated by considering a Taylor series expansion of the yield function as

$$\Delta\lambda = \dot{\lambda}\Delta t = \frac{f}{\eta_v}\overline{t} \tag{19}$$

where $\Delta t\,(= \Delta t^{(i+1)} = t^{(i+1)} - t^{(i)})$ is the time elapsed during an iteration of the correction loop. The term $\overline{t}$ represents instantaneous time (Ortiz and Simo 1986) given by

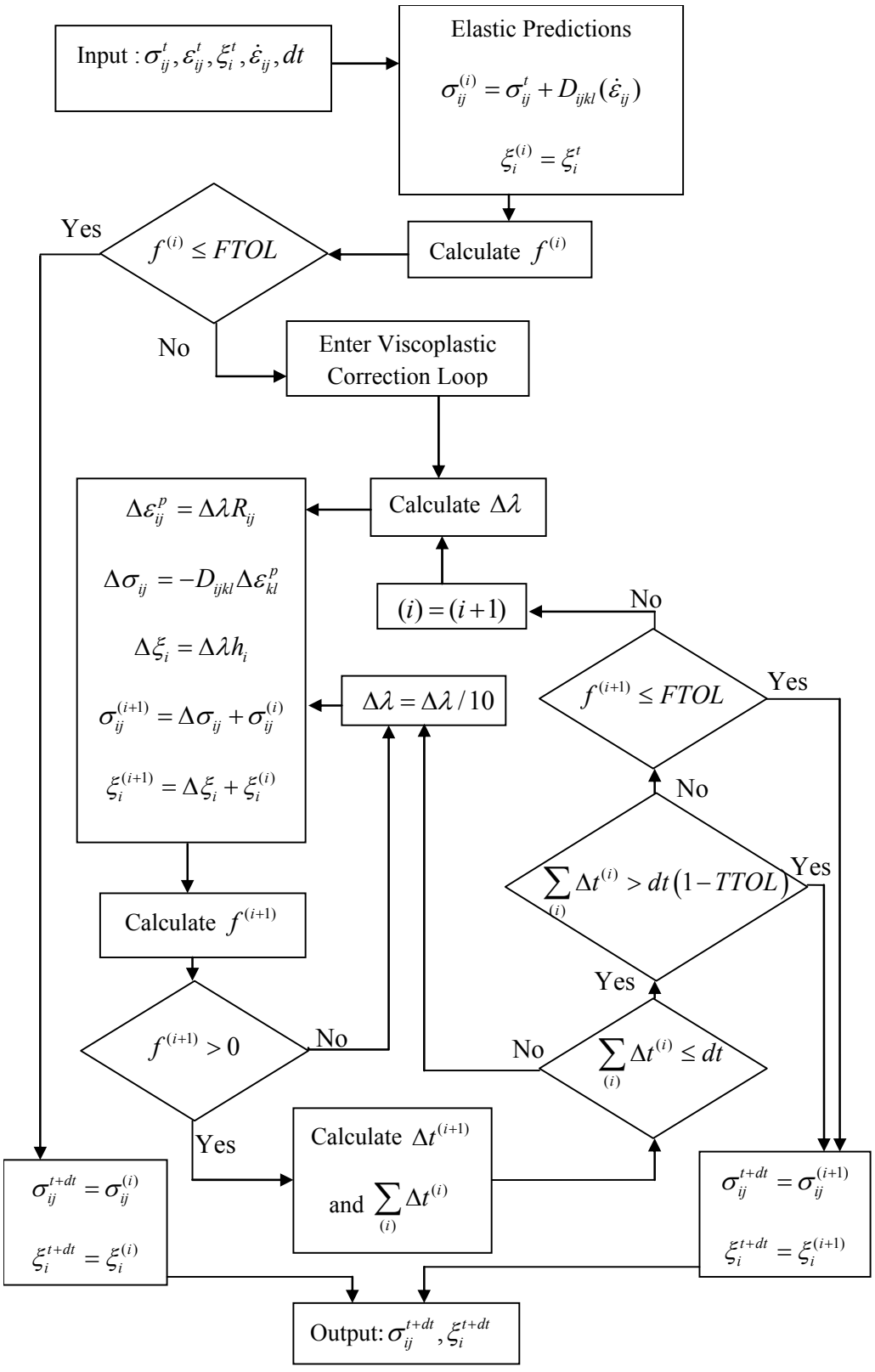

Figure 3. Cutting plane algorithm flow chart

$$\bar{t} = \frac{\eta_v}{\frac{\partial f}{\partial \sigma_{ij}} D_{ijkl} R_{kl} - K_P} \tag{20}$$

The value of $\Delta\lambda$ from equation (19) is used to quantify the change in the variables (e.g., σ_{ij} and ξ_i) between the iterations of the correction loop, and the updated values of stresses and hardening variables are calculated to obtain the updated yield function value $f^{(i+1)}$ (Higgins 2011). The iterations in the viscoplastic correction loop continue until the yield function value falls within the tolerance *FTOL* (i.e., $f^{(i+1)} \le FTOL$) or until the time increment *dt* is exhausted.

It is possible in the course of the viscoplastic correction that the position of the final, relaxed stress state is inside the yield surface. Theoretically, this condition (i.e., $f^{(i+1)} \le 0$) is not possible and it also gives rise to numerical problems. Hence, an additional check is done to make sure that the value of $f^{(i+1)} > 0$. Therefore, if the predicted value of $\Delta\lambda$ causes the overstress to move inside the yield surface resulting in $f^{(i+1)} \le 0$, then the iteration is rejected, σ_{ij} and ξ_i are returned to the values of the previous iteration and a decreased value of $\Delta\lambda$ is used to proceed further (the decreased value of $\Delta\lambda$ is assumed to be $\Delta\lambda/10$ in this study). It should be noted that decreasing the value of $\Delta\lambda$ does not affect the solution of the final stress value that is converged upon, it only affects the number of iterations required to reach the converged value.

The actual elapsed time Δt of an iteration of the correction loop is calculated from the previous and updated values of the yield function, $f^{(i)}$ and $f^{(i+1)}$, as (Ortiz and Simo 1986)

$$\Delta t = \overline{t} \ln\left(\frac{f^{(i)}}{f^{(i+1)}}\right) \tag{21}$$

When the summation of the elapsed time of the iterations in the correction loop $\sum_{(i)} \Delta t^{(i)}$ becomes equal to the time increment *dt* of the analysis, the relaxation time expires. Thus, when $\sum_{(i)} \Delta t^{(i)} = dt$, the program exits the viscoplastic correction loop.

If after updating the stresses it is found that $\sum_{(i)} \Delta t^{(i)} > dt$, then too much time has elapsed and the current stress state is invalid. If that happens (i.e., if $\sum_{(i)} \Delta t^{(i)} > dt$), then the set of iterations is rejected — the algorithm returns to the previous values of stresses, hardening variables and state parameters, and starts again with a decreased value of $\Delta\lambda$. This process is continued until $\sum_{(i)} \Delta t^{(i)}$ falls within some tolerance of dt. This tolerance was so set that, in order for the program to exit the correction loop, the total elapsed time has to meet the condition $(1 - TTOL)dt < \sum_{(i)} \Delta t^{(i)} \le dt$ where $TTOL = 0.0001$.

It is clear from the above discussion that the algorithm exits the viscoplastic correction loop if the time increment *dt* is exhausted (i.e., if $\sum_{(i)} \Delta t^{(i)} = dt$) or if the viscoplastic stress state is sufficiently close to the yield surface (i.e., $f^{(i+1)} \le FTOL$). If the time increment gets exhausted before the condition $f^{(i+1)} \le FTOL$ is satisfied, then the stress state remains outside the yield surface as the algorithm moves to the next time *t* + *dt*. If, on the other hand, the condition $f^{(i+1)} \le FTOL$ is satisfied, then the algorithm is moved to the next time *t* + *dt* even before the time increment *dt* is exhausted because, in

the remainder of the time available for viscoplastic corrections, the change in the values of the stresses and hardening variables is minimal.

The implementation of the cutting plane algorithm is done in conjunction with an error control algorithm (Higgins 2011). The error control algorithm limits the magnitude of the time increment *dt* by comparing the stresses obtained by executing the cutting plane algorithm with *dt* as the time increment with the stresses obtained after two successive executions of the cutting plane algorithm each with a time increment of *dt*/2. If the difference between the stresses obtained from these two sets of solution is large, then the time step *dt* is decreased until the difference falls within a tolerable limit.

MODEL CALIBRATION AND VALIDATION

The developed constitutive model was used to simulate the drained triaxial compression tests and SHPB tests performed on Ottawa and Fontainebleau sands. The parameters used in the simulations are given in Table 1. The parameters used for the Ottawa sand were mostly obtained from Loukidis (2006) in which the calibrations were done based on triaxial compression tests (Carraro 2004, Murthy et al. 2006), triaxial extension tests (Murthy et al. 2006) and bender element tests (Carraro 2004). Modifications were made to the values of the critical-state parameters Γ, λ, and ζ so as to better capture the sand behavior at high strain rates and at high pressures (> 100 MPa) experienced in the SHPB tests. The new values of these parameters were obtained by optimizing the critical-state line to capture the behavior of the SHPB tests (Veyera and Ross 1995) while maintaining good agreement with the triaxial tests (Higgins 2011). The model calibration for Fontainebleau sand was done using the data from triaxial compression tests (Luong 1980, Dano et al. 2004, Hircher et al. 2008, Gaudin et al.

2003), triaxial extension tests (Luong 1980), torsional hollow cylinder tests (Georgiannou and Tsomokos 2008) and SHPB tests (Semblat et al. 1999).

Table 1. Parameters used in the simulations of Ottawa and Fontainebleau sand tests

Parameters	Ottawa Sand	Fontainebleau Sand
ν	0.15	0.3
C_g	611	650
e_g	2.17	2.17
n_g	0.437	0.437
Γ	0.85	2.0
λ	0.12	1.1
ζ	0.275	0.1
M_{cc}	1.31	1.157
k_b	1.9	3.0
h_1	2.2	1.2
h_2	0.24	0.2
e_{lim}	0.81	1.0
m	0.05	0.05
C_1	0.71	0.71
n_s	0.35	0.35
D_0	1.31	0.5
k_d	2.2	2.0
μ	1.2	1.2
η_v (kPa-sec)	50	5
Maximum Void Ratio $e_{\max}$	0.78	0.863
Minimum Void Ratio $e_{\min}$	0.48	0.523

Simulation of Triaxial Tests

The triaxial tests were simulated using a single, axisymmetric element in the finite element software Abaqus version 6.9 (Abaqus User's Manual 2009). The element was fixed against vertical movement along its bottom edge. The element was loaded with an initial hydrostatic pressure maintained as a constant load on the outer radial edge. The analysis was driven by applying displacements at the top edge of the element.

The simulations of the triaxial compression tests for Ottawa sand are based on the laboratory test data of Carraro (2004). The initial confining pressure in these tests was set at 100 kPa and the tests were run at the initial void ratio e_0 = 0.7 and 0.55. Figures 4(a) and (b) show the deviatoric stress versus axial strain and the volumetric strain versus axial strain plots, respectively. It is evident that the constitutive model differentiates between dilative and contractive behavior of sand at different void ratios and provides a reasonable match with the experimental results. A similar match between the experimental and simulation results was obtained for Fontainebleau sand under triaxial compression tests (Higgins 2011).

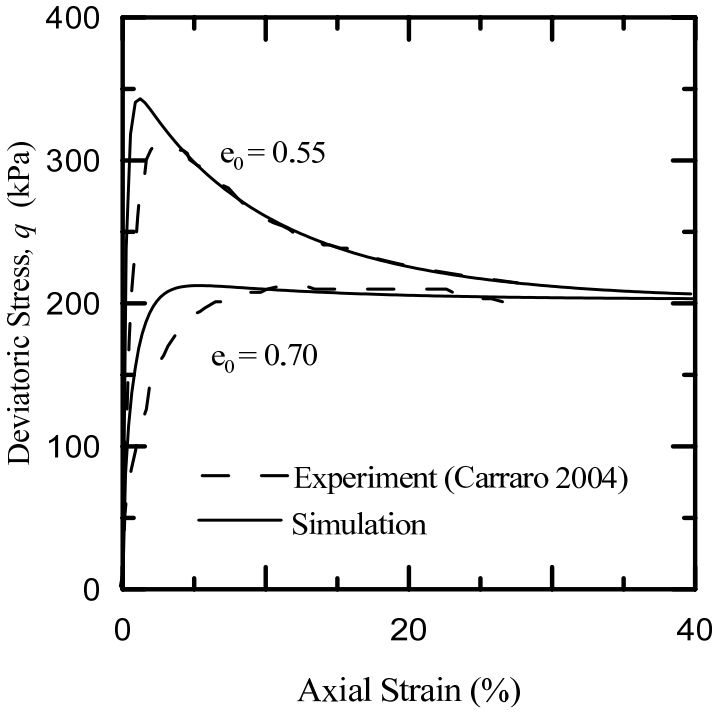

(a)

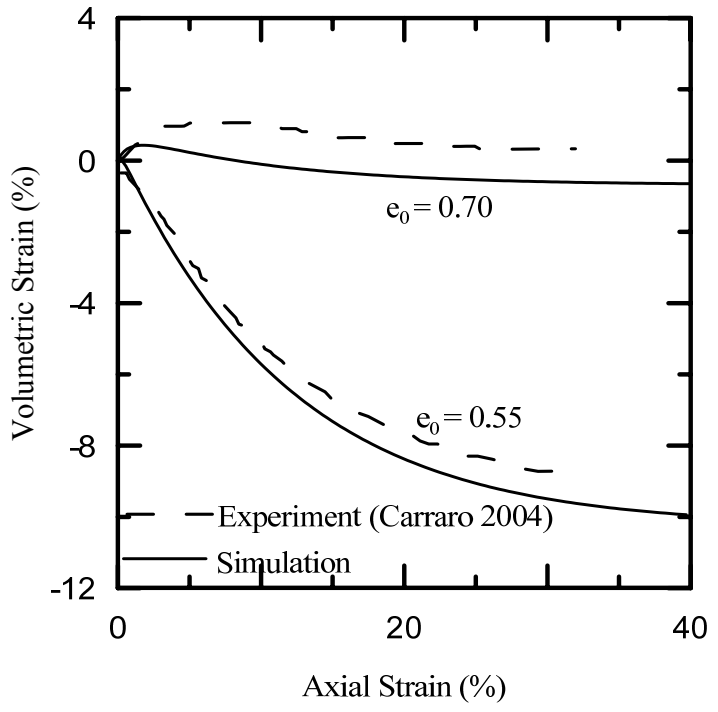

(b)

Figure 4. (a) Deviatoric stress versus axial strain and (b) volumetric strain versus axial strain of Ottawa sand in drained triaxial tests with an initial confining pressure of 100 kPa

Simulation of SHPB Tests

The SHPB tests were also simulated using Abaqus. Four separate axisymmetric parts were created to simulate the striker bar, incident bar, output bar and the soil sample. The magnitude of the impulse wave was controlled by adjusting the initial velocity of the striker bar in Abaqus. In the actual experiments, the soil sample was confined against transverse displacement with a rigid collar. In the simulations, this effect was accounted for by directly applying boundary conditions to the soil elements so that the transverse displacement was restrained. The contact planes between the bars and the specimen were modeled using hard contact.

The SHPB tests on dry Ottawa sand were conducted by Veyera and Ross (1995). The strain rates achieved in these tests were between 1000/sec and 2000/sec. The Ottawa sand samples were compacted to a void ratio of 0.545. The samples had a diameter of 5.08 cm and lengths L_0 = 1.27 cm and 0.635 cm. The SHPB set up had stainless steel bars with a diameter of 5.08 cm. The material properties used for simulating the bars are Young's modulus = 207 GPa and density = 7850 kg/m^3. The striker bar had a length of 0.635 m, the incident bar had a length of 3.66 m and the output bar had a length of 3.35 m. By using an initial striker bar velocity of 12 m/sec in the simulations, an impulse wave comparable to the one reported by Veyera and Ross (1995) was produced.

Figure 5 shows the axial stress versus axial strain plots of the SHPB tests performed on Ottawa sand samples. The stress-strain plots show that a sample subjected to a faster strain rate achieves greater stresses. There is a reasonably good match between the experimental data and simulation results.

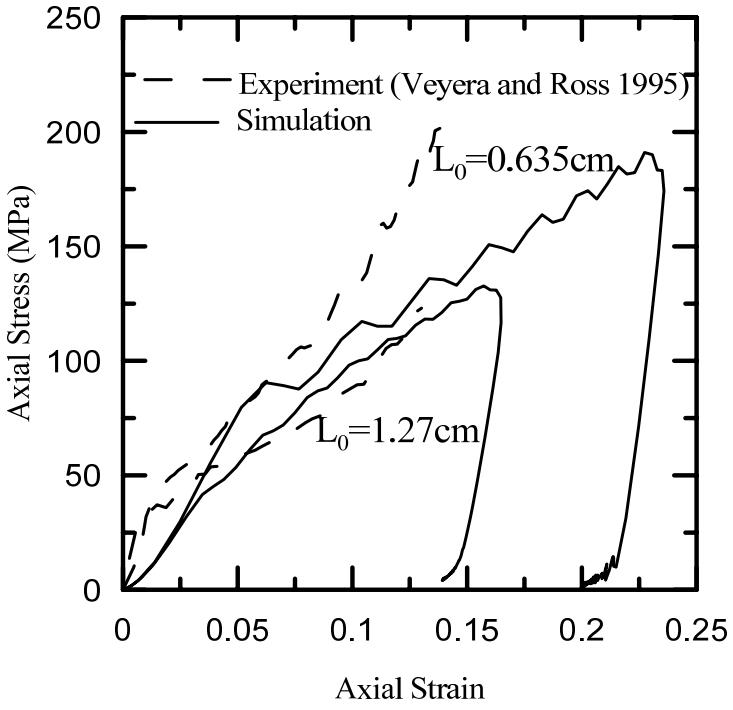

Figure 5. Axial stress versus axial strain of Ottawa sand in split Hopkinson pressure bar tests

The simulations for Fontainebleau sand are based on the SHPB tests performed by Semblat et al. (1999) on dry samples. Semblat et al. (1999) ran tests with different lengths of the sand sample and with different velocities of the striker bar to create different strain rates in the samples. The stress-strain plots are shown in Figure 6 for tests performed with samples of length 10 cm and diameter 40 mm with the initial striker bar velocity V_0 = 6.8 m/sec, 11.6 m/sec and 19.8 m/sec. The samples had an initial void ratio of 0.667. The bars used in the SHPB set up had a diameter of 40 mm, Young's modulus of 70 GPa and density of 2820 Kg/m^3. The striker bar had a length of 0.85 m while the impulse and output bars each had a length of 2 m. The simulated stress-strain plots match the experimental results well.

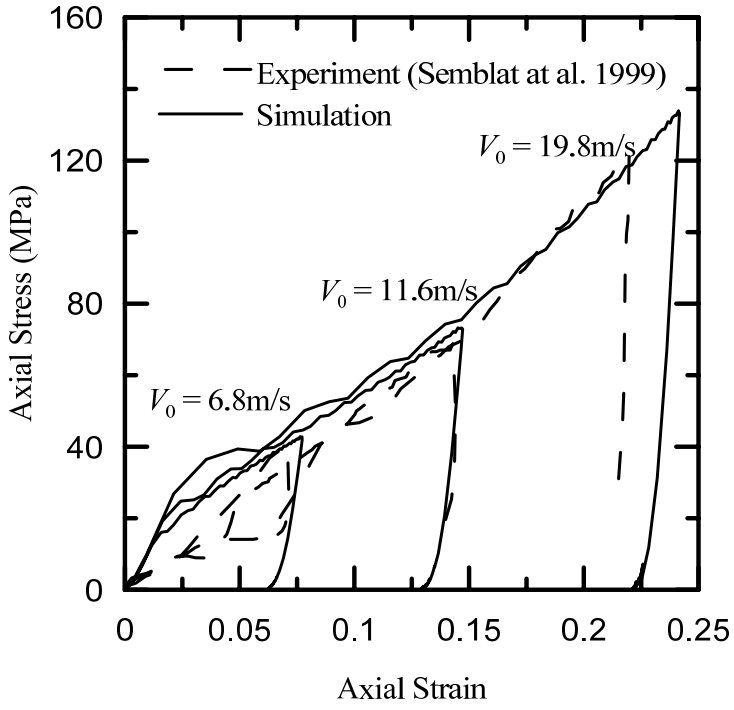

Figure 6. Axial stress versus axial strain of Fontainebleau sand in split Hopkinson pressure bar tests

FINITE ELEMENT ANALYSIS OF TUNNELS SUBJECTED TO BLAST

The developed constitutive model was used to analyze underground tunnels subjected to internal blast loads. The purpose of these simulations is to demonstrate the ability of the constitutive model to simulate real field problems and to gain insights into how soil adjacent to a tunnel behaves when a blast occurs inside the tunnel.

Two dimensional plane strain FE analyses were performed using rectangular, plain strain, reduced integration (CPE4R) elements in Abaqus, and the resulting stress waves propagating through the surrounding soil were simulated. Two geometries were considered in this study. In one case, the center line of the tunnel was at 5 m below the ground surface and, in the other case, the tunnel center line was at a depth of 10 m. For

both the cases, the tunnel had an internal radius of 2.85 m with a 0.15 m thick concrete lining.

A typical finite element mesh is shown in Figure 7. In order to save on the computation time, only one half of the actual domain was analyzed by imposing a symmetry boundary condition along the left vertical boundary of the mesh. The top horizontal boundary was free to displace while the bottom horizontal boundary was restrained against both vertical and horizontal displacements. Vertical displacements were allowed along the left and right vertical boundaries but not horizontal displacements. The bottom horizontal boundary and the right vertical boundary were located at sufficient distances so that they had no impact on the results of the analysis — the results were obtained at a time when the stress wave from the blast was far from these boundaries. The mesh for the 5 m deep tunnel consists of 1624 elements and 1718 nodes and the mesh for the 10 m deep tunnel consists of 2306 elements and 2414 nodes.

It was assumed in the FE analyses that the grounds surrounding the tunnels have properties similar to Ottawa and Fontainebleau sands. Two different relative density (D_R) values, 50% (which corresponds to an initial void ratio $e_0 = 0.63$ for Ottawa sand and to $e_0 = 0.69$ for Fontainebleau sand) and 80% (which corresponds to $e_0 = 0.54$ for Ottawa sand and to $e_0 = 0.59$ for Fontainebleau sand), were considered. The concrete lining of the tunnels was simulated using the concrete damaged plasticity model built into Abaqus. The material properties used for concrete are Young's modulus = 31 GPa, Poisson's ratio = 0.15, compressive yield strength = 13 MPa and tensile yield strength = 2.9 MPa. The stresses generated in the ground due to the explosions inside the tunnels were investigated along a horizontal path AB shown in Figure 8.

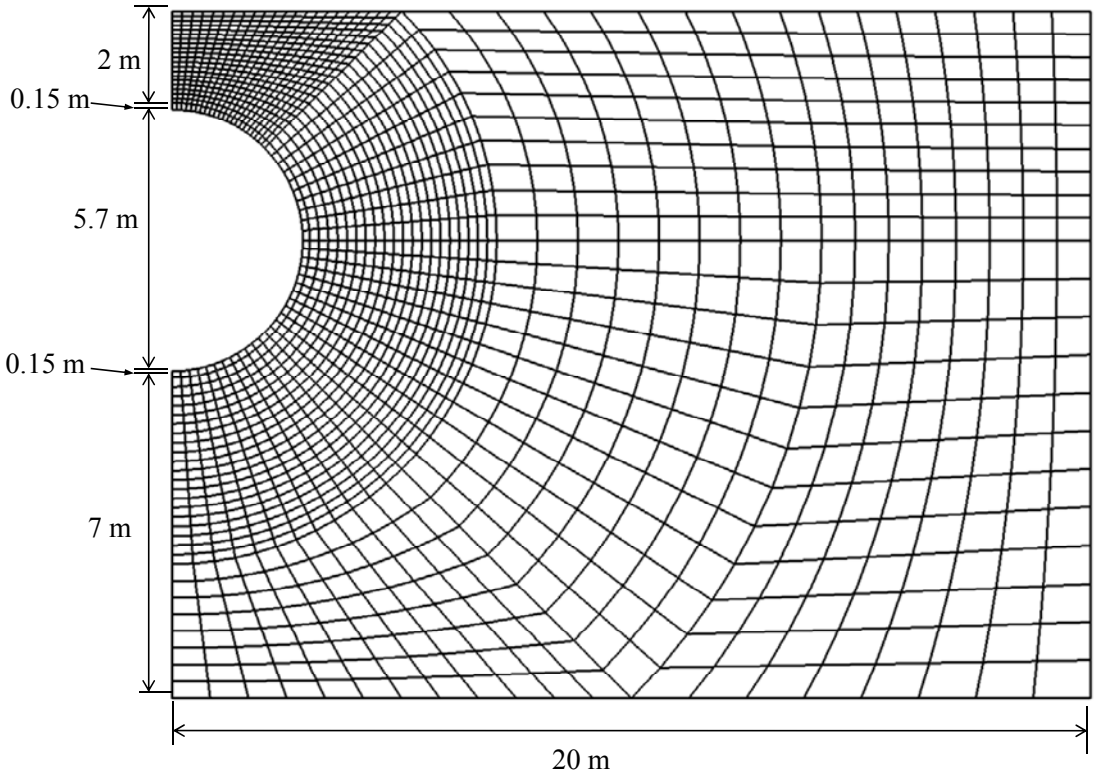

Figure 7. A typical finite element mesh used in the analysis of tunnels (the tunnel center line is at a depth of 5 m below the ground surface)

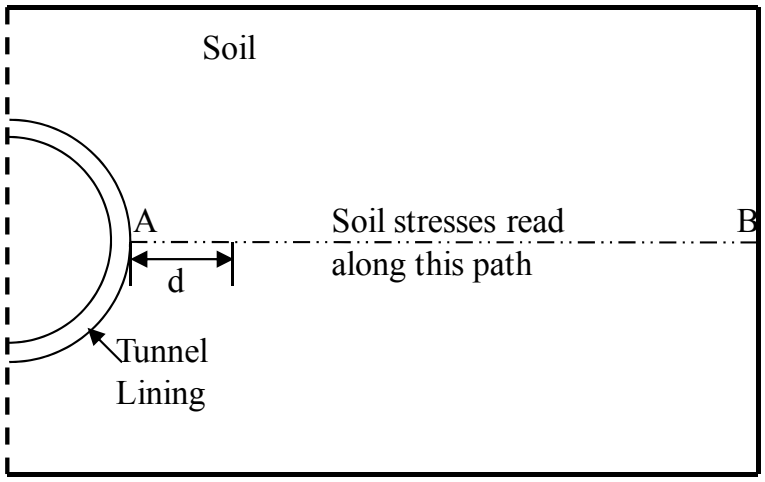

Figure 8. Path AB along which stresses in soil are studied

Blasts due to the explosive C4 were simulated using the Jones-Wilkens-Lee (JWL) equation-of-state model (Lee et al. 1973) with the assumption that the explosive material is located at the center line of the tunnel. The radius of the explosive material assumed before detonation is 0.1 m — this corresponds to a mass of 50.3 kg/m. Air elements were used to mesh the interior of the tunnel and the dynamic pressure acting on the inner tunnel wall due to the explosions were generated as a function of time as shown in Figure 9 (Higgins 2011).

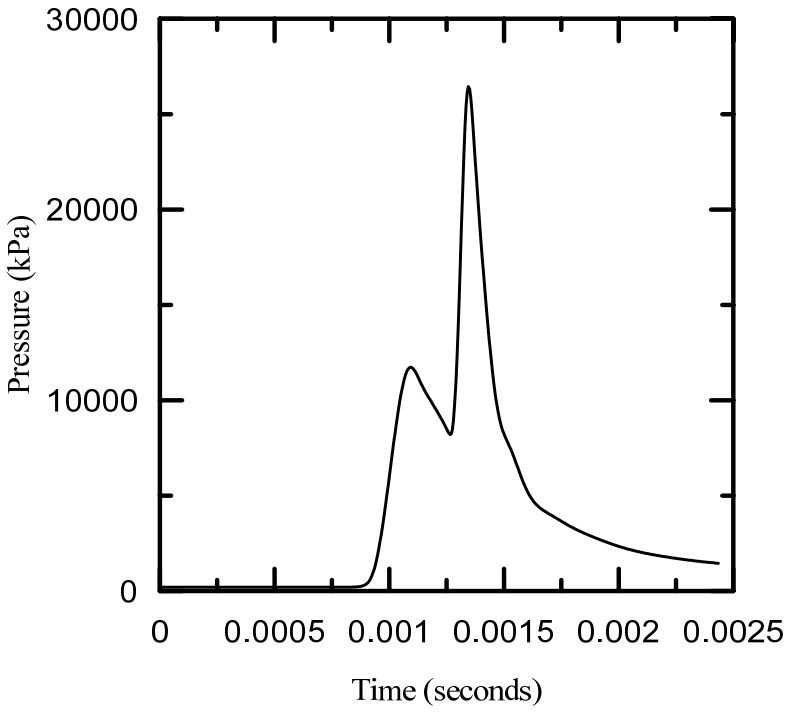

Figure 9. Pressure amplitude curve for the explosive C4 of radius 0.1 m in a tunnel with an internal radius of 2.85 m

Figures 10(a) and (b) show the variations of the mean and deviatoric stresses with time at three different points in the ground at a distance d = 0.5 m, 1.5 m and 2.5 m from

the interface of the tunnel and ground along the horizontal path AB (Figure 8). The center line of the tunnel is located at a depth of 10 m below the ground surface. The ground is assumed to have the same properties as that of Ottawa sand with D_R = 50% and 80%. As the stress wave propagates, the stresses at different horizontal distances increase, reach a maximum and then decrease. The maximum values of the stresses experienced by a point in soil decreases as the distance of the point from the tunnel increases. In the denser sand (i.e., for D_R = 80%), the wave propagates faster and the stresses reach higher peaks.

Figures 11(a) and (b) compare the temporal variations of the mean and deviatoric stresses at three different points along the path AB for Ottawa sand Fontainebleau sands with D_R = 80%. It is evident that the wave speed and the peak mean stress are greater in Fontainebleau sand than in Ottawa sand. These results were obtained for the 10 m deep tunnel.

Figures 12(a) and (b) show the spatial variations of the maximum mean and deviatoric stresses along the horizontal path AB for the 10 m deep tunnel. In order to obtain the plots, the mean and deviatoric stress versus time data were recorded for all the elements along the path AB and the maximum stresses experienced over time in each element are plotted as a function of the distance of the element from the outer edge of the tunnel lining. The rate of spatial dissipation of the maximum mean stress is comparable for both the sands while the spatial dissipation of the maximum deviatoric stress is faster in Ottawa sand.

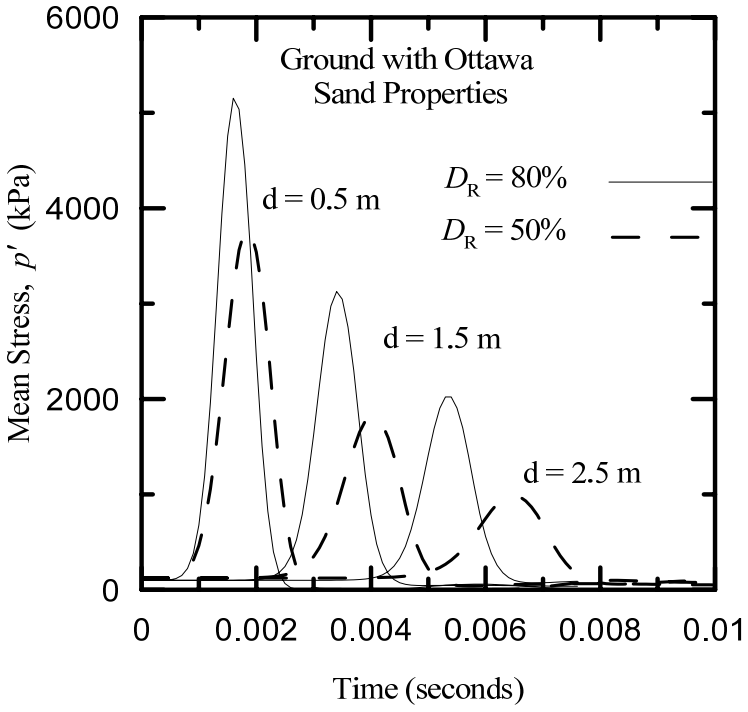

(a)

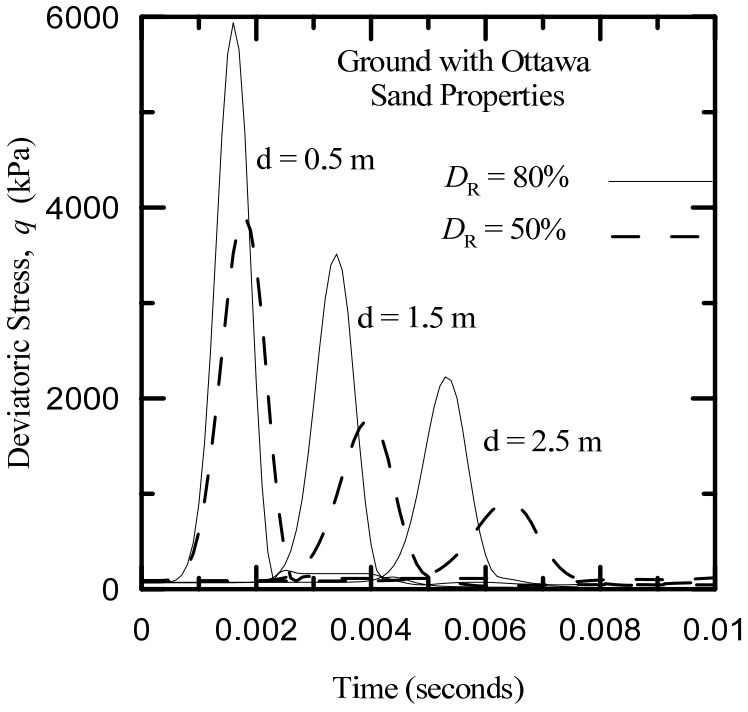

(b)

Figure 10. Temporal variation of (a) mean stress and (b) deviatoric stress at three points in the ground adjacent to 10 m deep tunnels in Ottawa sand subjected to explosions of C4

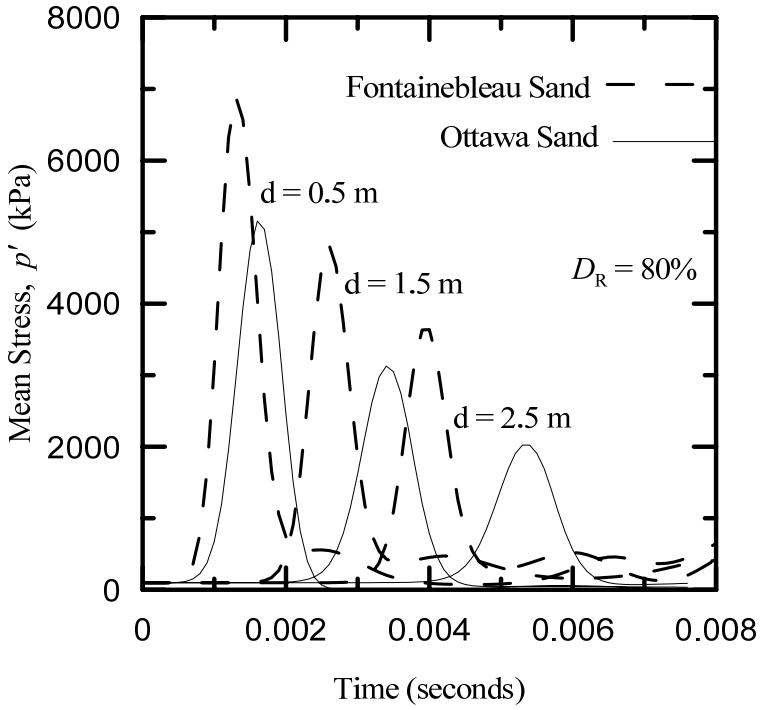

(a)

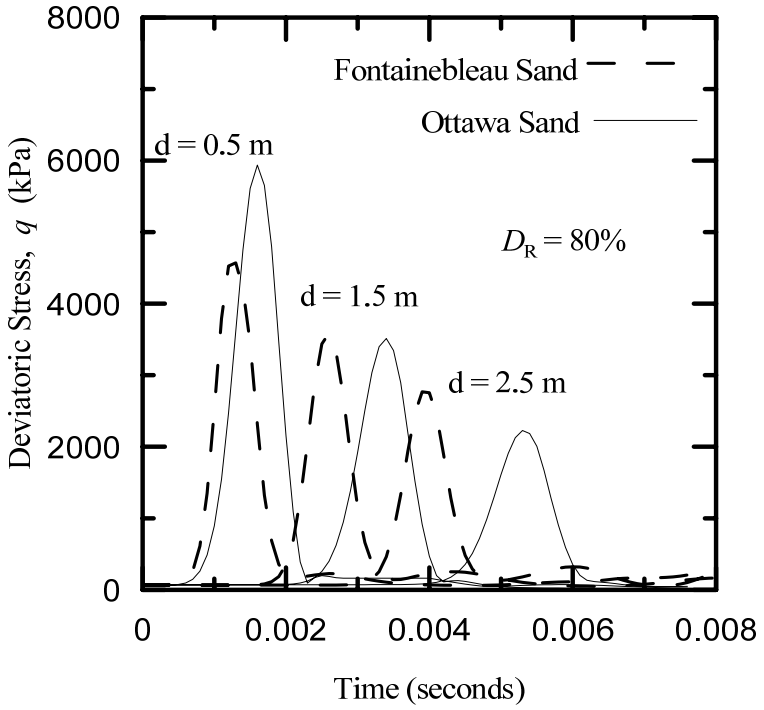

(b)

Figure 11. Temporal variation of (a) mean stress and (b) deviatoric stress at three points in the ground adjacent to 10 m deep tunnels in Ottawa and Fontainebleau sands subjected to explosions of C4

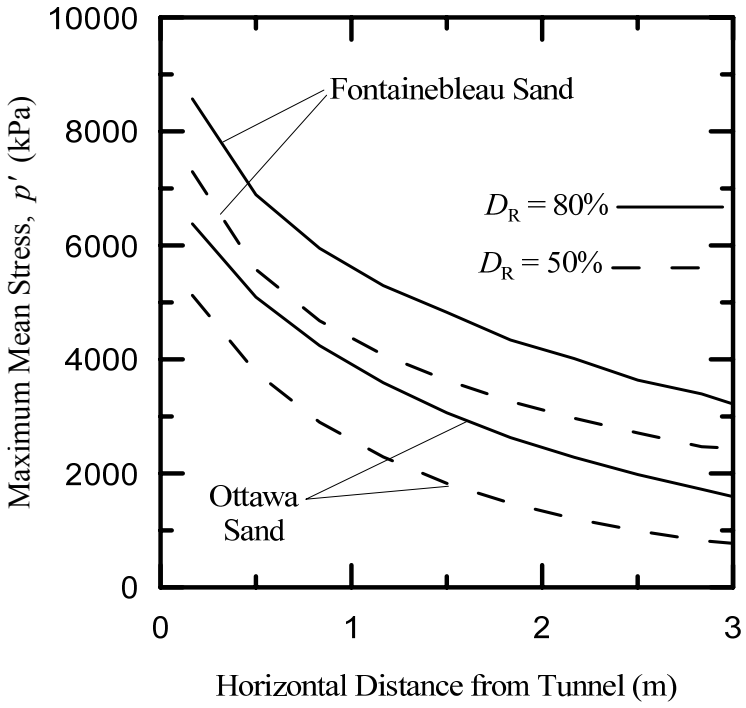

(a)

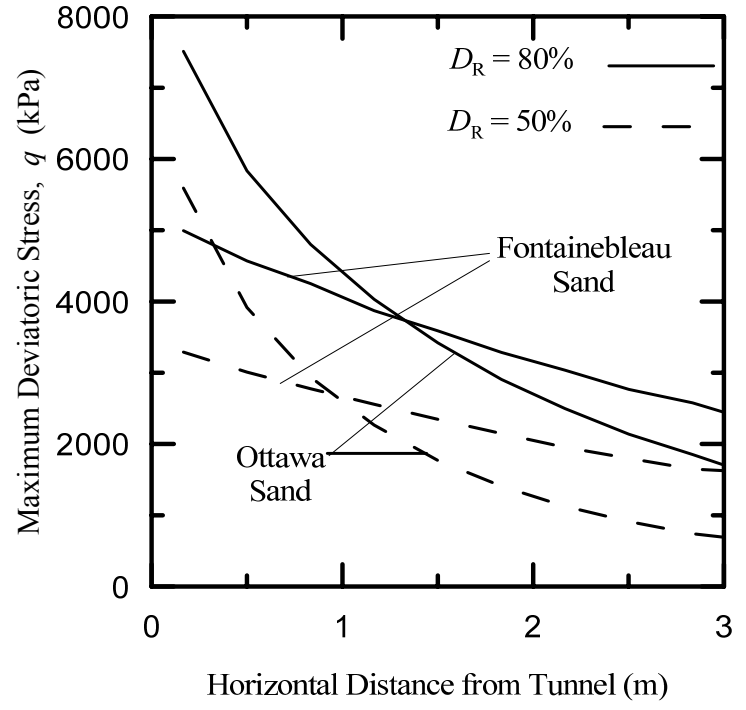

(b)

Figure 12. Spatial variation of (a) maximum mean stress and (b) maximum deviatoric stress in the ground adjacent to 10 m deep tunnels subjected to C4 explosions

Figures 13 (a) and (b) show the p'-q and e-p' relationships of a soil element on the path AB immediately adjacent to the 10 m deep tunnel. The normalized void ratio e/e_0 (e_0 is the initial void ratio) is plotted in Figure 13(b). It is interesting to note that the changes in the stresses due to blast are quite large but the changes in the void ratio are rather insignificant.

Figures 14(a) and (b) show how the depth of tunnel affects the ground response. For these figures, the simulations were performed for Ottawa sand with tunnels having center lines at the depths of 5 m and 10 m from the ground surface. It is evident that the spatial dissipations of the maximum mean and deviatoric stresses (along the path AB) are faster for the shallower tunnel.

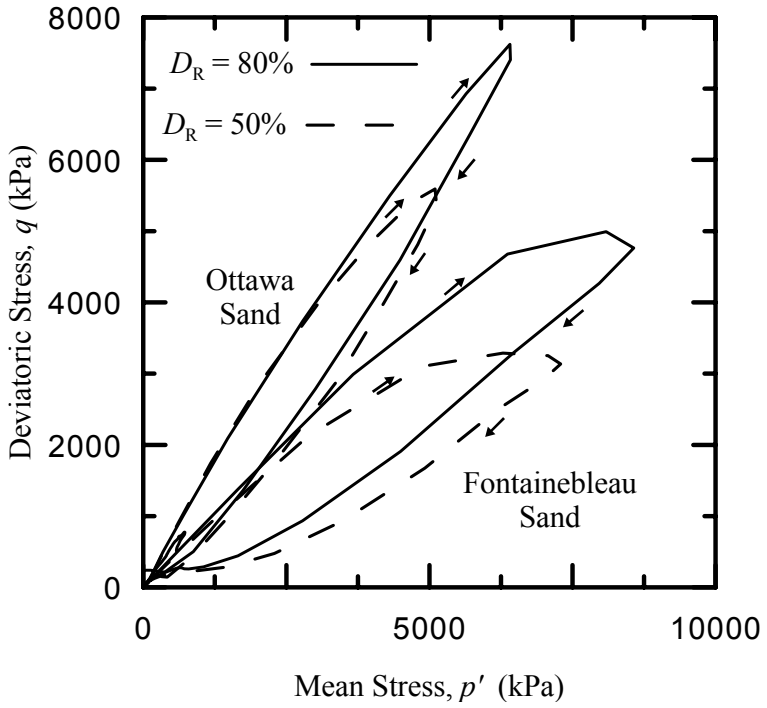

(a)

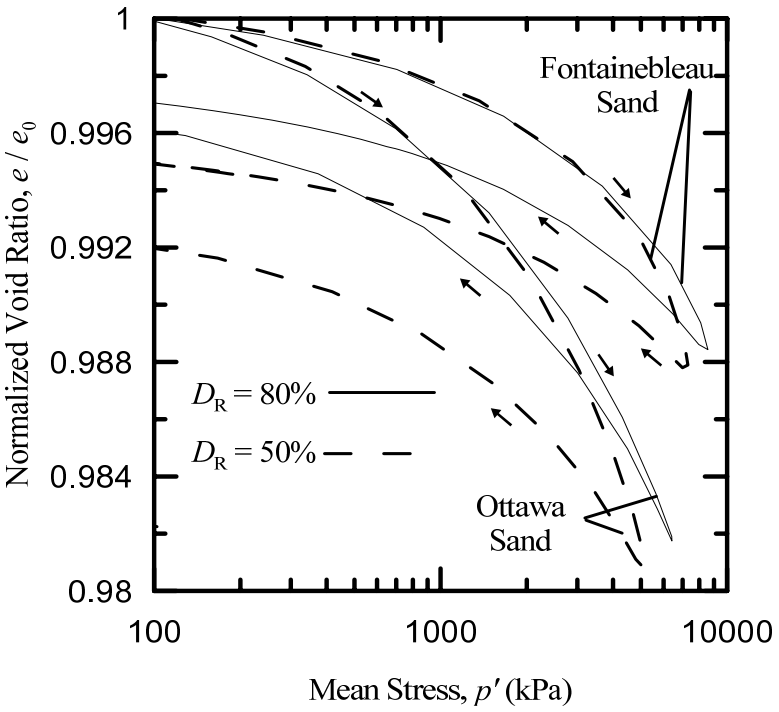

(b)

Figure 13. (a) Mean stress versus deviatoric stress and (b) normalized void ratio versus mean stress for the soil element horizontally adjacent to 10 m deep tunnels exploded with C4

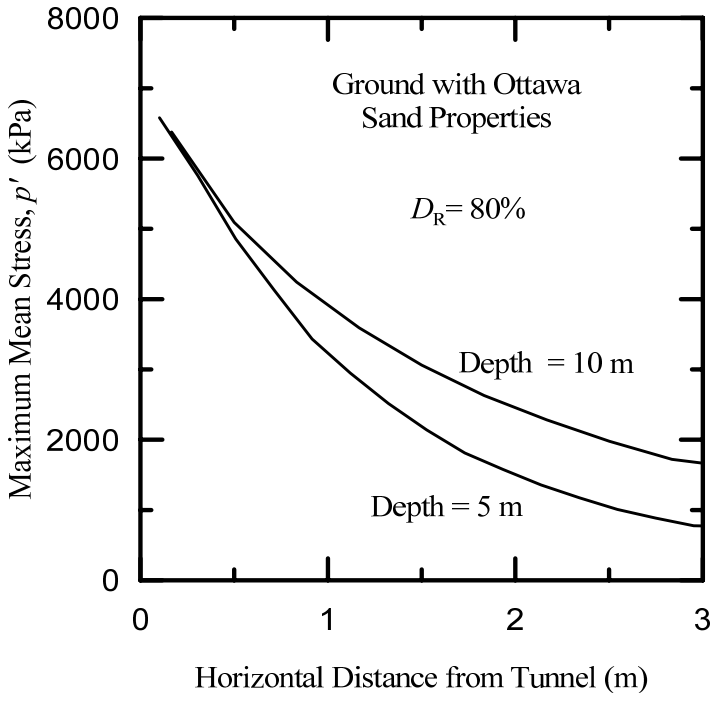

(a)

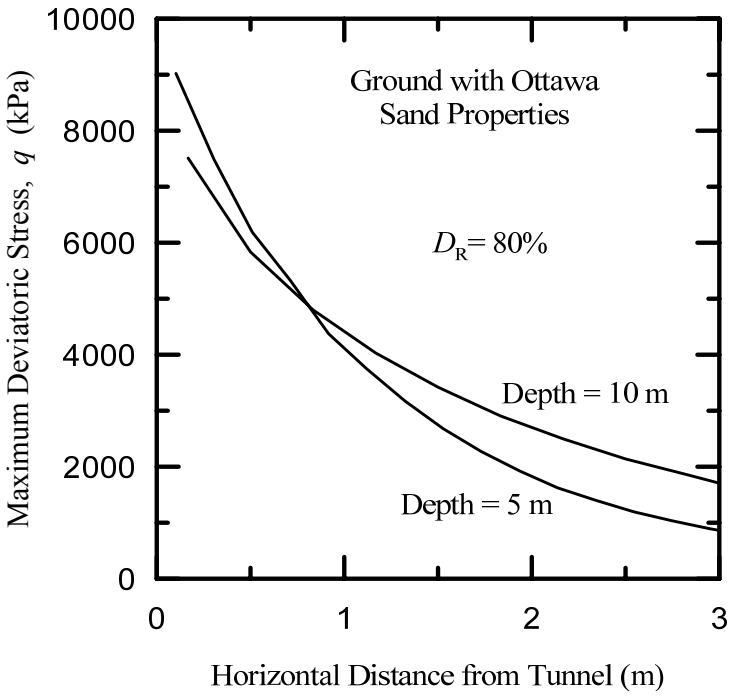

(b)

Figure 14. (a) Maximum mean stress and (b) maximum deviatoric stress versus horizontal distance from 5 m and 10 m deep tunnels in Ottawa sand subjected to C4 explosions

CONCLUSIONS

In this report, a constitutive model was developed which is capable of simulating the high strain-rate behavior of sands under multi-axial loading conditions. The model is developed from the modified bounding surface plasticity model of Manzari and Dafalias (1997) in conjunction with the overstress theory of viscoplasticity (Perzyna 1963, 1966). The developed model is capable of distinguishing and simulating the behavior of contractive and dilative sands under rate-independent and high-rate loads. The parameters of the model were calibrated to simulate the mechanical behavior of Ottawa and Fontainebleau sands. The critical-state parameters of the model were adjusted to account for the large stresses experienced in the split Hopkinson pressure bar tests and during blast loading in soil. The model was implemented in the finite element software Abaqus using the cutting plane algorithm and was used to analyze static and transient problems. Static drained triaxial tests and dynamic split Hopkinson pressure bar tests on Ottawa and Fontainebleau sands were simulated for the validation of the model.

The constitutive model was subsequently applied in two dimensional (plane strain) finite element analysis of tunnels subject to blast loads. Circular underground tunnels constructed in sandy soils were subjected to blasts caused by the explosion of C4. The blast was simulated using the JWL equation-of-state model. It was found that the type and relative density of sand and the depth of tunnel influence the propagation of the blast induced stress waves through the ground. The wave speed was found to be greater in Fontainebleau sand than in Ottawa sand. The rate of spatial dissipation of the maximum mean stress was comparable for both the sands while the spatial dissipation of the maximum shear stress was faster in Ottawa sand. The speed of propagation of the

stress waves is faster in denser sands. The rates of spatial dissipation of the maximum mean and deviatoric stresses are greater in a 5 m deep tunnel than in a 10 m deep tunnel.

REFERENCES

Abaqus v6.9 user's manual (2009), *Abaqus Inc., DS Simulia*, Providence, Rhode Island, USA.

An, J., Tuan, C. Y., Cheeseman, B. A., and Gazonas, G. A. (2011). "Simulation of soil behavior under blast loading." *International Journal of Geomechanics.* Vol. 11 (4), p. 323 – 334.

Been, K. and Jefferies, M. G. (1985). "A state parameter for sands." *Géotechnique*, Vol. 35 (2), p. 99-112.

Bessette, G. C.(2008). "Modeling blast loading on buried reinforced concrete structures with Zapotec." *Journal Shock and Vibration*, Vol.15 (2), p. 137-146.

Carraro, J. A. H. (2004). "Mechanical behavior of silty and clayey sands." *Ph.D. Thesis*, Purdue University, West Lafayette, Indiana, USA.

Dafalias, Y. F. (1982). ''Bounding surface elastoplasticity-viscoplasticity for particulate cohesive media.'' *International Union of Theoretical and Applied Mechanics Conference on Deformation and Failure of Granular Materials* (P. A. Vermeer and H. J. Luger, eds.), p. 97–107.

Dafalias, Y. F., Papadimitriou, A. G. and Li, X. S. (2004). "Sand plasticity model accounting for inherent fabric anisotropy." *Journal of Engineering Mechanics*, *ASCE*, Vol. 130 (11), p. 1319-1333.

Feldgun, V. R., Kochetkov, A. V., Karinski, Y. S., and Yankelevsky, D. Z. (2008a). "Internal blast loading in a buried lined tunnel." *International Journal of Impact Engineering*, Vol.35, p.172–183.

Feldgun, V. R., Kochetkov, A. V., Karinski, Y. S. and Yankelevsky, D. Z. (2008b). "Blast response of a lined cavity in a porous saturated soil." *International Journal of Impact Engineering*, Vol.35 (9), p. 953-966.

Felice, C. W. (1985). "The response of soil to impulse loads using the S.H.P.B technique." *Ph.D. Thesis*. University of Utah, Salt Lake City, Utah, USA..

Hardin, B. O. and Richart, F. E., Jr. (1963). "The nature of stress-strain behavior of soils." *Journal of Soil Mechanics and Foundations Division, ASCE,* vol. 89 (1), p. 33-65.

Higgins, W. T. (2011). "Development of a high strain-rate constitutive model for sands and its application in finite element analysis of tunnels subjected to blast." *M.Sc. Thesis*, University of Connecticut, Storrs, Connecticut, USA.

Jackson, J. G., Rohani, B., and Ehrgott, J. Q. (1980) "Loading rate effects on compressibility of sand.", *Journal of Geotechnical Engineering Division*, Vol. 106 (8), p. 839–852.

Karinski, Y. S., Feldgun, V. R. and Yankelevsky, D. Z. (2008). "Explosion-induced dynamic soil-structure interaction analysis with the coupled Godunov-variational difference approach." *International Journal for Numerical Methods in Engineering*, Vol.77 (6), p. 824 – 851.

Krieg, R. D. (1972) "A simple constitutive description for cellular concrete." Sandia National Laboratories, Albuquerque, New Mexico, USA.

Laine, P. and Sandvik. A. (2001). "Derivation of mechanical properties for sand." *Proceedings of the 4th Asia–Pacific conference on Shock and Impact Loads on Structures*. Singapore, p. 361–368.

Loukidis, D. (2006). "Advanced constitutive modeling of sands and applications to foundation engineering." *Ph.D. Thesis*, Purdue University, West Lafayette, Indiana, USA.

Loukidis D, Salgado R. (2009) "Modeling sand response using two-surface plasticity." *Computers and Geotechnics*, Vol. 36 (1–2), p. 166–186.

Lu, Y., Wang, Z. and Chong, K. (2005). "A comparative study of buried structure in soil subjected to blast load using 2D and 3D numerical simulations." *Soil Dynamics and Earthquake Engineering*, Vol.25, p. 275–288.

Murthy, T. G., Loukidis, D., Carraro, J. A. H, Prezzi, M. & Salgado, R. (2006). "Undrained monotonic behavior of clean and nonplastic silty sands." *Géotechnique,* Vol 57 (3), p. 273–288.

Nagy, N., Mohamed, M. and Boot, J.C., (2010) "Nonlinear numerical modeling for the effects of surface explosions on buried reinforced concrete structures." *Geomechanics and Engineering*, Vol. 2, (1), p.1-18.

Ortiz, M. and Simo, J. C. (1986), "An analysis of a new class of integration algorithms for elastoplastic constitutive relations." *International Journal for Numerical Methods in Engineering,* Vol.23, p.353-366.

Perzyna, P. (1963). "The constitutive equations for rate sensitive plastic materials." *Quarterly of Applied Mathematics,* Vol. 20, p. 321-332.

Perzyna, P. (1966). “Fundamental problems in viscoplasticity.” *Advances in Applied Mechanics*, Vol. 9, p. 244–377.

Seed, H. B. and Lundgren, R. (1954). “Investigation of the effect of transient loading on the strength and deformation characteristics of saturated sands.” *Proceedings of 57th Annual Meeting of the Society*, *ASTM,* West Conshohocken, Pennsylvania, USA, no. 54, p. 1288-1306.

Semblat J. F., Luong M. P., Gary G. (1999). “3d-Hopkinson bar: new experiments for dynamic testing on soils.” *Soils and Foundations,* Vol. 39 (1) p. 1-10.

Song, B, Chen, W., Luk, L. (2009) “Impact compressive response of dry sand.” *Mechanics of Materials*, Vol 41 (6), p. 777 – 785.

Tong, X. and Tuan, C. (2007). “Viscoplastic cap model for soils under high strain rate loading.” *Journal of Geotechnical and Geoenvironmental Engineering*, *ASCE*, Vol. 133 (2), p. 206-214.

Veyera, G. E. and Ross, C. A. (1995). "High strain rate testing of unsaturated sands using a split-Hopkinson pressure bar." *Proceedings of 3rd International Conference on Recent Advances in Geotechnical Earthquake Engineering and Soil Dynamics*, St-Louis, Missouri, USA, p. 31-34.

Wang, Z., Hao, H. and Lu, Y. (2004). “A three-phase soil model for simulating stress wave propagation due to blast loading.” *International Journal of Numerical and Analytical Methods in Geomechanics*, Vol.28, p. 33–56.

Whitman, R. V. and Healy, K. A. (1962). “Shear strength of sands during rapid loading.” *Journal of the Soil Mechanics and Foundations Division*, *ASCE,* Vol. 88 (SM2), p. 99-132.

Yamamuro, J. A. and Abrantes, A. E. (2003). "Behavior of medium sand under very high strain rates." *Proceedings of 1st Japan-U. S. Workshop on Testing, Modeling, and Simulation*, Boston, Massachusetts, USA, p. 61-70.

Yang, Y., Xie, X. Wang, R., (2010). "Numerical simulation of dynamic response of operating metro tunnel induced by ground explosion." *Journal of Rock Mechanics and Geotechnical Engineering,* Vol. 2 (4), p. 373-384.